



HAL
open science

Ultrasound scattering from cell-pellet biophantoms and ex vivo tumors provides insight into the cellular structure involved in scattering

Pauline Muleki Seya, William O'Brien

► **To cite this version:**

Pauline Muleki Seya, William O'Brien. Ultrasound scattering from cell-pellet biophantoms and ex vivo tumors provides insight into the cellular structure involved in scattering. *IEEE Transactions on Ultrasonics, Ferroelectrics and Frequency Control*, 2021, 69 (2), pp.637-649. 10.1109/TUFFC.2021.3130682 . hal-03538526

HAL Id: hal-03538526

<https://hal.science/hal-03538526>

Submitted on 7 Mar 2022

HAL is a multi-disciplinary open access archive for the deposit and dissemination of scientific research documents, whether they are published or not. The documents may come from teaching and research institutions in France or abroad, or from public or private research centers.

L'archive ouverte pluridisciplinaire **HAL**, est destinée au dépôt et à la diffusion de documents scientifiques de niveau recherche, publiés ou non, émanant des établissements d'enseignement et de recherche français ou étrangers, des laboratoires publics ou privés.

Ultrasound scattering from cell-pellet biophantoms and *ex vivo* tumors provides insight into the cellular structure involved in scattering

Pauline Muleki-Seya and William D. O'Brien, Jr. *Life Fellow IEEE*

Abstract—The histologically identifiable cellular structure(s) involved in ultrasonic scattering is(are) yet to be uniquely identified. The study quantifies six possible cellular scattering parameters, namely, cell and nucleus radii and their respective cell and nucleus volume fractions as well as a combination of cell and nucleus radii and their volume fraction. The six cellular parameters are each derived from four cell lines (4T1, JC, LMTK and MAT) and two tissue types (cell-pellet biophantom and *ex vivo* tumor). Optical histology and quantitative ultrasound (QUS), both independent approaches, are used to yield these cellular parameters. QUS scatterer parameters are experimentally determined using two ultrasonic scattering models: the spherical Gaussian model (GM) and the structure factor model (SFM) to yield insight about scattering from nuclei only and cells only. GM is a classical ultrasonic scattering model to evaluate QUS parameters and is well adapted for diluted media. SFM is adapted for dense media to estimate reasonably well scatterer parameters of cellular structures from *ex vivo* tissue. Nucleus and cell radii and volume fractions are measured optically from histology. They were used as inputs to calculate BSC for scattering from cells, nuclei, and both cells and nuclei. The QUS-derived scatterers (radii, volume fractions) distributions were then compared to the optical histology scatterer parameters derived from these calculated BSCs. The results suggest scattering from cells only (LMTK and MAT) or both cells and nuclei (4T1 and JC) for cell-pellet biophantoms and scattering from nuclei only for tumors.

Index Terms—Backscatter coefficient, Cell-pellet biophantoms, *Ex vivo* tissues, Scattering source

I. INTRODUCTION

Cell-pellet (CP) biophantoms are composed of densely packed cells and are often used to mimic tumors in quantitative ultrasound (QUS) studies. These CP-biophantom-based QUS studies have been used to address tissue characterizations [1]–[7] or monitor cell death applications [8], [9] by apoptosis [10] or mitotic arrest [11]. QUS provides information about tissue microstructure and is based on analyses of ultrasonic backscattered signals or more specifically the backscatter coefficient (BSC). Then, ultrasonic scatterer parameters (radius, acoustic concentration, volume fraction, relative impedance contrast) are estimated by fitting a theoretical

BSC derived from an ultrasonic scattering model to the experimentally derived BSC.

To determine if CP biophantoms provide adequate tumor models, it is necessary to demonstrate that the histologically identifiable cellular structure(s) involved in ultrasonic scattering is(are) closely related between biophantoms and tumors. However, the ultrasonic scattering structure(s) at the cellular level is(are) still not identified. The challenge may result from inadequate ultrasonic scattering models. Classically employed scattering models (Spherical Gaussian model, Fluid Sphere model, etc.) are adapted for dilute media that satisfy the condition of random and independent distribution of scatterers. However, the dilute-media condition is not satisfied for dense-media CP biophantoms [3] or tumors that have densely packed cells [9]. The Structure Factor Model (SFM) is better adapted for dense media [12] because, unlike the classical ultrasonic models that consider only incoherent scattering by summing the contributions from individual ultrasonic scatterers, the SFM considers also the scatterers' interactions using a statistical mechanics structure factor [13], [14]. A previous study [12] suggested that the main ultrasonic scattering structure from canine liver was the hepatocyte nucleus and from HT29 mouse tumors was the whole cell. Another study [15] suggested that the nucleus was the dominant scattering source in rabbit liver based on a 3-D impedance map study. By comparing cell-pellet biophantoms and corresponding isolated nuclei biophantoms with different nuclei size, Taggard et al. [16], concluded that the BSC was correlated to the size of nuclei. Other studies based mainly on the effect of apoptosis on ultrasonic backscattering have suggested the nucleus was the major scattering source [17]–[19].

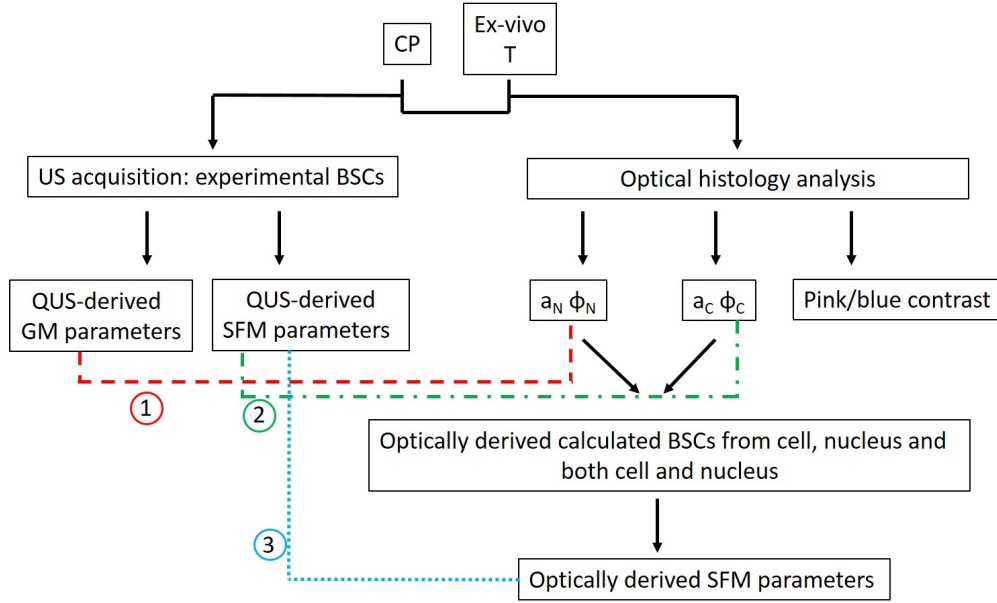
There is significant scientific value to elucidate the ultrasonic scattering structure(s), particularly at the cellular scale. Fundamentally, this is of great relevance for developing novel imaging and diagnostic capabilities from first principles. For example, if CP biophantoms are equivalent models of tumors for tissue characterization applications, then simpler non-animal-based experimental approaches might become readily available, thus broadening the capability and productivity of laboratory-based studies.

The study's objective is to gain insight into the cellular structure(s) that is(are) involved in ultrasonic scattering.

This research was supported by NIH grants R37EB002641 and R01CA226528. Corresponding author: Pauline Muleki-Seya.

Pauline Muleki-Seya is with Univ Lyon, INSA-Lyon, Université Claude Bernard Lyon 1, UJM-Saint Etienne, CNRS, Inserm, CREATIS UMR 5220, U1206, F-69100, Villeurbanne, France. (e-mail: pauline.muleki-seya@creatis.insa-lyon.fr).

William D. O'Brien, Jr is with the Bioacoustics Research Laboratory, Department of Electrical and Computer Engineering, University of Illinois at Urbana-Champaign, 306 N. Wright St., Urbana, IL 61801, USA.



- ① Comparison between GM parameters and nucleus parameters from histology: scattering from nuclei.
- ② Comparison between SFM parameters and cell parameters from histology: scattering from cells.
- ③ Comparison between QUS-derived and optically-derived SFM parameters: scattering from both nuclei and cells.

Fig. 1. Schematic diagram of the study. a_N , ϕ_N , a_C , ϕ_C denote the radii and volume fractions from nuclei and cells.

For that, the same four cell lines are utilized in both CP biophantoms and *ex vivo* tumors (T). There are three main study objectives (Figure 1). 1) Determine if nuclei only or cells only are involved in ultrasonic scattering from the CP biophantoms and *ex vivo* tumors. For that, the QUS-derived scatterer parameters from experimental BSC outcomes using Spherical Gaussian model (GM) and SFM are compared to the nucleus and cell radii and volume fractions (respectively, track 1 and 2, Figure 1); this approach is based on the following assumptions. If scattering from nuclei only is considered, then the BSC would consist of an incoherent contribution, and the GM should provide reasonably accurate parameter estimates of nuclei. If scattering from cells only is considered, then the BSC would consist of both incoherent and coherent contributions, and the SFM should provide reasonably accurate parameter estimates of cells. The approach in this part of the study is similar to our previous study [12]. 2) Evaluate if both cells and nuclei are involved in ultrasonic scattering from CP biophantoms and *ex vivo* tumors. For that, the optical histology-measured parameters (mean nucleus and cell radii and volume fractions) from CP biophantoms and *ex vivo* tumors are used as inputs to evaluate BSCs with a simple scattering model from cells, nuclei and both cells and nuclei. Then, optical histology-derived scatterer parameters are estimated and compared to the QUS-derived outcomes (track 3, Figure 1). This model and its methodology are the main contributions of this study. 3) Determine if the main ultrasonic scatterers are different between the four cell lines from CP biophantoms and *ex vivo* tumors. For that, the optically derived nucleus and cell

Term	Definition
Experimental BSC	BSC evaluated from experimental ultrasonic acquisition
QUS-derived parameters	Scatterer parameters evaluated from experimental BSC: scatterer radius and acoustic concentration using GM and scatterer radius, volume fraction and relative impedance contrast using SFM
Optical histology-measured parameters	Cells and nuclei radii and volume fractions measured on histological images
Calculated BSC	BSC evaluated with SFM model using the mean optical-histology parameters as income
Optical histology-derived parameters	Scatterer parameters evaluated from calculated BSC: scatterer radius, volume fraction and relative impedance contrast using SFM

TABLE I

MAIN TERMS USED IN THE STUDY AND THEIR DEFINITIONS.

radii and their volume fractions are compared among the different cell lines. Also, pink and blue contrasts from nuclei and cells optically derived from H&E staining are evaluated to provide relative information about their acoustic impedance.

II. MATERIAL AND METHODS

A. Glossary

The main terms used in the study and their definitions are summarize in Table I.

B. CP biophantoms and ex vivo tumors (T)

The CP biophantoms are composed of a large number of densely packed cells without any supportive background materials. Four tumor cell lines are used to create the CP biophantoms: 13762 MAT B III (MAT) mammary adenocarcinoma (ATCC CRL-1666), 4T1 mammary carcinoma (ATCC CRL-2539), JC mammary adenocarcinoma (ATCC CRL-2116) and LMTK soft-tissue sarcoma (ATCC CCL-1.3), denoted MAT, 4T1, JC and LMTK, respectively. The experimental procedure to fabricate CP biophantoms has been described in [2]. 3 MAT, 16 4T1, 10 JC, and 15 LMTK independent CP replicates are ultrasonically scanned and analyzed.

Tumors are grown in mice and rats (Harlan Laboratories, Inc., Indianapolis, IN) using the same CP cell lines: 13 Fischer 344 rats (MAT tumors), 20 BALB/c mice (13 mice with 4T1 tumors and 7 mice with JC tumors) and 8 Nude-Foxn1nu mice (LMTK tumors). The MAT, 4T1, JC and LMTK cells are injected into rats or mice. The animals are anesthetized with isoflurane before subcutaneous and bilateral cell injection into the mammary fat pad. Injection volume is 100 μL (containing 500 cells for MAT and 4T1, 2×10^5 cells for JC and 10^4 cells for LMTK) or 50 μL (containing 10^5 MAT cells). Tumor size was regularly monitored *in vivo* both manually and using a Vevo 2100 system (VisualSonics Inc., Toronto, ON, Canada). Tumors were allowed to grow to about 5 mm in diameter. The animals were then euthanized via CO_2 and the tumors were excised and placed on a planar Plexiglas plate. 18 MAT, 22 4T1, 10 JC, and 13 LMTK independent tumor replicates were excised, ultrasonically scanned, and analyzed.

The experimental protocol was approved by the Institutional Animal Care and Use Committee of the University of Illinois and satisfied all campus and National Institutes of Health rules for the humane use of laboratory animals. Animals were housed in an approved Association for Assessment and Accreditation of Laboratory Animal Care (Rockville, MD) animal facility, and provided food and water ad libitum.

C. QUS acquisition from CP biophantoms and ex vivo tumors

A single-element, weakly focused 40-MHz transducer (High Frequency Transducer Resource Center, USC, Los Angeles, CA, -10 dB bandwidth of 25–55 MHz) was used to scan CPs and Ts. The transducer was interfaced with a UTEX UT340 pulser/receiver (UTEX Scientific Instruments Inc., Mississauga, ON, Canada) that operated in the pitch-catch mode. A 50DR-001 BNC attenuator (JFW Industries Inc., Indianapolis, IN) was connected to the pulser to attenuate the driving pulse to avoid transducer saturation. An RDX-6 diplexer (Ritec Inc., Warwick, RI) was used to separate the transmitted and received signals because only the transmitted signal needed to be attenuated. The received radiofrequency (RF) signals were acquired using a 10-bit Agilent U1065A-002 A/D (Agilent Technologies, Santa Clara, CA) set to sample at 1 GHz. The ultrasonic transducer was moved using a precision motion control system (Daedal Parker Hannifin Corporation, Irwin, PA) with a linear spatial accuracy of 1 μm . The samples were placed on the Plexiglas plate during ultrasonic scans. The scans were performed at room

	CP		T	
	α (dB/cm)	n	α (dB/cm)	n
4T1	0.13 ± 0.03	1.42 ± 0.05	0.14 ± 0.03	1.42 ± 0.05
JC	0.14 ± 0.06	1.43 ± 0.08	0.21 ± 0.05	1.32 ± 0.08
LMTK	0.18 ± 0.03	1.34 ± 0.04	0.13 ± 0.04	1.46 ± 0.07
MAT	0.06 ± 0.01	1.58 ± 0.02	0.18 ± 0.07	1.41 ± 0.07

TABLE II

MEAN ATTENUATION COEFFICIENTS AND STANDARD DEVIATIONS FOR EACH TISSUE TYPE (CP AND T). THE ATTENUATION COEFFICIENTS CORRESPOND TO αf^n WHERE f DENOTES THE FREQUENCY.

temperature in a small tank filled with DPBS (Dulbecco's phosphate-buffered saline) for CP or saline for T.

Ultrasonic attenuation and BSC measurements were both performed for all CP and T samples. Attenuation values were acquired using an insertion-loss broadband technique [20], and used to yield accurate BSC values because of the large attenuation values at the ultrasonic frequencies used herein. The insertion loss was determined by comparing the power spectra of the echoes reflected off the Plexiglas surface with and without the sample inserted in the ultrasonic propagation path. The effect of DPBS or saline attenuation was compensated for. The attenuation (dB/cm) of each sample was generated by averaging the attenuation obtained from 36 independent locations across the sample, and the mean attenuation coefficients summarize in Table II. The BSC scanning procedure has been described in [2]. For each sample, 11 independent scans were recorded. A mean BSC was estimated for each of the 11 scans by averaging the BSCs from different regions-of-interest (ROIs) within that scan (ROIs correspond to 75%-overlapped regions with dimensions 0.56 x 0.56 mm, equivalent to 15 x 15 wavelengths at 40 MHz). Then, for each CP and T sample, 11 mean BSCs were used to estimate the ultrasonic scatterer parameters.

D. Optical evaluations from histology images

Immediately after ultrasonic scanning, the sample was placed into a histology processing cassette and fixed by immersion in 10% neutral-buffered formalin (pH 7.2) for a minimum of 12 h for histopathologic processing. The sample was then embedded in paraffin, sectioned, mounted on a glass slide, and stained with hematoxylin and eosin (H&E) for histopathologic evaluation by light microscopy (Olympus BX-51, Optical Analysis Corporation, Nashua, NH). Examples of histology images for each CP and T cell lines are shown in Figure 2.

From the optical histology images, nucleus and cell radii were estimated. For each CP and T, at least 3 histology images were selected to measure several nuclei areas using the ImageJ software. Assuming that the nuclei and cells have circular shapes, their corresponding radii were computed from the area estimates. The mean nucleus and cell radii were estimated by measuring at least 150 of the largest nuclei and cells. From 2-D histology images, the nucleus and cell sizes are likely underestimated because the microtome's blade does not generally intersect the nucleus and/or cell

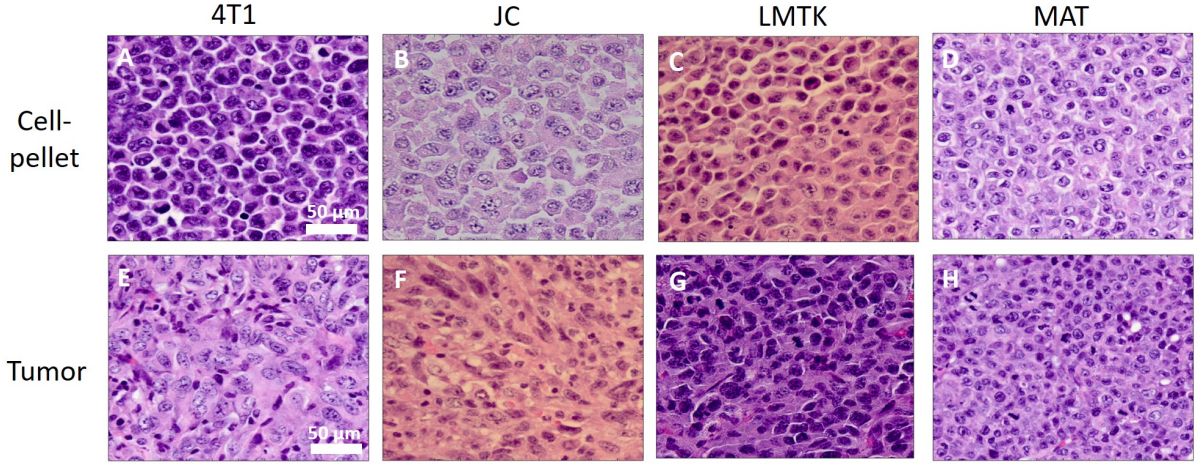


Fig. 2. Examples of *H&E*-stained histology images of 4T1, JC, LMTK and MAT CP and T. Scale is the same for all images

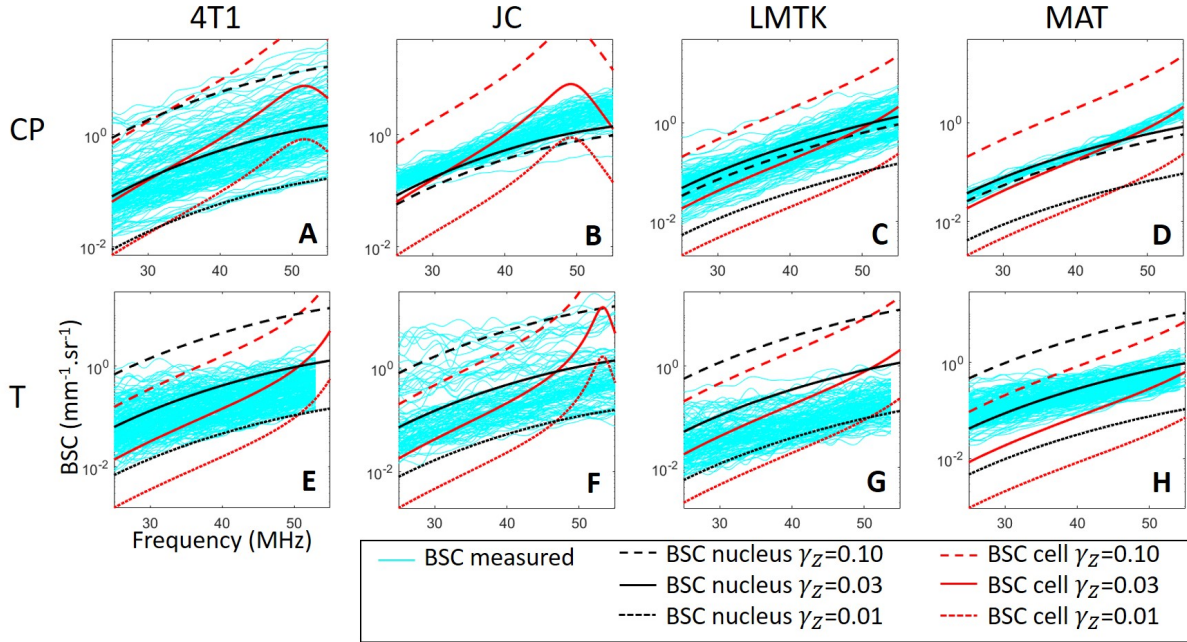


Fig. 3. QUS-derived mean BSCs (11 BSCs for each sample) for 4T1, JC, LMTK and MAT CP and T (cyan lines). Superimposed on these plots are calculated BSCs from nuclei only (black continuous and dashed lines) and cells only (red continuous and dashed lines) using mean optical histology-derived a and ϕ estimates for each cell line and for three values of relative impedance contrast γ_Z (0.1, 0.03 and 0.01). CP denotes cell-pellet biophantom and T denotes tumor. Note, BSCs are plotted in log scale for a sake of readability.

centers, thus yielding circular structures with sizes smaller than the actual nuclei or cells. To limit this underestimation of the nucleus and cell radii, only the largest nuclei and cells were measured. Nucleus radii were evaluated for all four cell lines. Cell radii were evaluated for 4T1, JC, and LMTK CP. However, it was not possible to evaluate the cell radii for MAT CP and also for MAT, 4T1, JC and LMTK T because the cytoplasm's contours were difficult to identify accurately.

The nucleus and cell volume fractions were approximated from the 2-D optical histology images. The number of nuclei N was calculated in the histology image area A_{im} . To obtain estimates of nucleus volume fractions (respectively, cell

volume fractions), ϕ_N (ϕ_C), the volume occupied by nuclei (cells) was divided by the volume of the image using the estimated diameter of a cell d_C as the thickness dimension for the nucleus and cell volume fractions:

$$\phi_N = \frac{NV_N}{A_{im}d_C}, \quad \phi_C = \frac{NV_C}{A_{im}d_C} \quad (1)$$

where V_N and V_C denote the nucleus and cell volumes assuming spherical shapes of nuclei and cells, respectively. This procedure was used for the nucleus volume fraction estimation of each cell line and the final values were an average from 3 histology images. As LMTK and MAT nucleus radii were similar in size, the LMTK cell radius was used for the MAT cell radius. As cell radii were missing

for T, cell radii evaluated from CP were used as cell radii for T.

Ultrasonic scatterer parameters related to acoustic impedance from nuclei and cells were estimated from the *H&E*-stained histology images. *H&E* staining yields cytoplasm pink and nucleus blue with the intensity of pink or blue reflecting the protein or nucleic acid concentration, respectively [21]. A higher protein concentration in the medium appears pink and a higher nucleic acid concentration appears blue. Color intensity variation of this staining is interpreted as a difference in acoustic impedance. Pink and blue contrast values were estimated from cytoplasm and nuclei, respectively. The pink contrast (blue contrast, respectively) corresponds to the intensity value in the first RGB channel (third RGB channel, respectively) from RGB histology images. This pink contrast (blue contrast, respectively) was estimated for cytoplasm and nuclei on 5 CP and 5 T histology images. The contrast was then averaged and normalized over the sum of the intensity values from the first, second and third channels of the RGB image.

E. QUS models

The ultrasonic parameters from two QUS models are compared: the spherical Gaussian model (GM) and the Structure Factor Model (SFM). For the GM, the BSC is modelled using a spatial autocorrelation function describing the size, shape, acoustic properties, and distribution of the ultrasonic scatterers in the medium. The BSC was expressed as the product of the BSC in the Rayleigh limit and the backscatter form factor [22]. The form factor describes the frequency-dependent scattering in terms of the size, shape, and acoustic properties of the scatterers. The Gaussian form factor models a medium with continuous spatial changes in acoustic properties. The application of this model is valid for dilute media. The theoretical BSC using the GM formulation is given by [22]:

$$BSC_{GM}(k) = \frac{k^4 V_s^2 \eta_Z}{4\pi^2} e^{-0.827k^2 a_G^2}; \quad (2)$$

where k is the wavenumber, η_Z is the acoustic concentration, and a_G is the effective scatterer radius with $V_s = 4\pi a_G^3/3$. The unknown parameters are the scatterer radius a_G and the acoustic concentration η_Z . Note that the fluid sphere model [22], which is closer to the SFM, provides similar results as the GM. However, in this study, the GM is preferred to the fluid sphere model because the GM has been more frequently used in other studies.

The SFM is based on the assumption that, at high scatterer volume fractions (i.e., dense media), interference effects are mainly caused by correlations between the spatial positions of individual scatterers (discrete scatterer with impedance differing from that of a homogeneous background medium). By considering an ensemble of identical spheres of radius a , the theoretical BSC for the SFM formulation is given by [4], [14]:

$$BSC_{SFM}(k) = n \frac{k^4 V_s^2 \gamma_Z^2}{4\pi^2} \left[\frac{3}{(2ka)^3} j_1(2ka) \right]^2 S(k); \quad (3)$$

where V_s is the sphere volume and $n = \phi/V_s$ is the number density with ϕ the scatterer volume fraction, γ_Z the relative impedance contrast between scatterer and surrounding medium, and j_1 the spherical Bessel function of the first kind of order 1. S is the structure factor which can be analytically obtained as described in [4], eqs. (A1)–(A4) based on [23]. The unknown parameters are scatterer radius a , volume fraction ϕ , and relative impedance contrast γ_Z . The acoustic concentration for the SFM is calculated as: $\eta_Z = \phi \gamma_Z^2 / (4\pi a^3/3)$.

Estimated values of the QUS-derived parameters were determined by fitting the theoretical BSCs to the measured BSC_{meas} , i.e., by minimizing the cost function:

$$F = \frac{\sum_j \|BSC_{meas}(k_j) - BSC_{theo}(k_j)\|^2}{\sum_j BSC_{meas}(k_j)^2} \quad (4)$$

where BSC_{theo} is given by eq. 2 for GM and by eq. 3 for SFM. The cost functions are minimized over 25–55 MHz. The fitting procedure is performed using the minimization routine *fminsearch* without constraint in MATLAB (The MathWorks, Inc., Natick, MA). The minimum cost function is evaluated using 20 initial random conditions ($a \in [1 - 10] \mu\text{m}$, $\phi \in [0 - 0.7]$, $\gamma_Z \in [0.005 - 0.055]$, $\eta_Z \in [1 - 10] \text{dB}\cdot\text{mm}^{-3}$).

F. Optical histology-derived QUS evaluations of CP biophantoms and ex vivo T

As observed on the optical *H&E*-stained histology images (Figure 2), the nuclei colors in the RGB images are quite variable, thus suggesting that the nuclei acoustic impedance may be quite variable from one nucleus to another. Therefore, it is possible that for some cells, the main ultrasonic scattering sites are the nuclei and for others, the cells themselves. In this study, three potential sources of ultrasonic scatterers are considered: nuclei only, cells only and both nuclei and cells. Using the SFM (eq. 3), the calculated BSCs from nuclei only, cells only, and both nuclei and cells are generated from the optical histology-derived scatterer parameters. Then, the optical histology-derived scatterer parameters are compared against the QUS-derived scatterer parameters from experimental BSCs. In particular, we are interested in observing the scatterer outcome distributions (using the monodisperse SFM) in the presence of scattering from both cells and nuclei. The calculated BSCs from nuclei only BSC_N , cells only BSC_C , and both nuclei and cells BSC_{NC} are defined as:

$$BSC_N(k) = BSC_{SFM}(k, a_N, \phi_N) \quad (5)$$

$$BSC_C(k) = BSC_{SFM}(k, a_C, \phi_C) \quad (6)$$

$$BSC_{NC}(k) = w BSC_N(k) + (1 - w) BSC_C(k) \quad (7)$$

where the optical histology-derived parameters a_N , ϕ_N , a_C , ϕ_C are the radii and volume fractions from nuclei and cells, respectively, and w is the nucleus/cell scattering ratio: $w=0$ corresponds to scattering from cells only and $w=1$ corresponds to scattering from nuclei only. A relative impedance contrast, γ_Z , of 0.03 for 4T1, JC, LMTK and

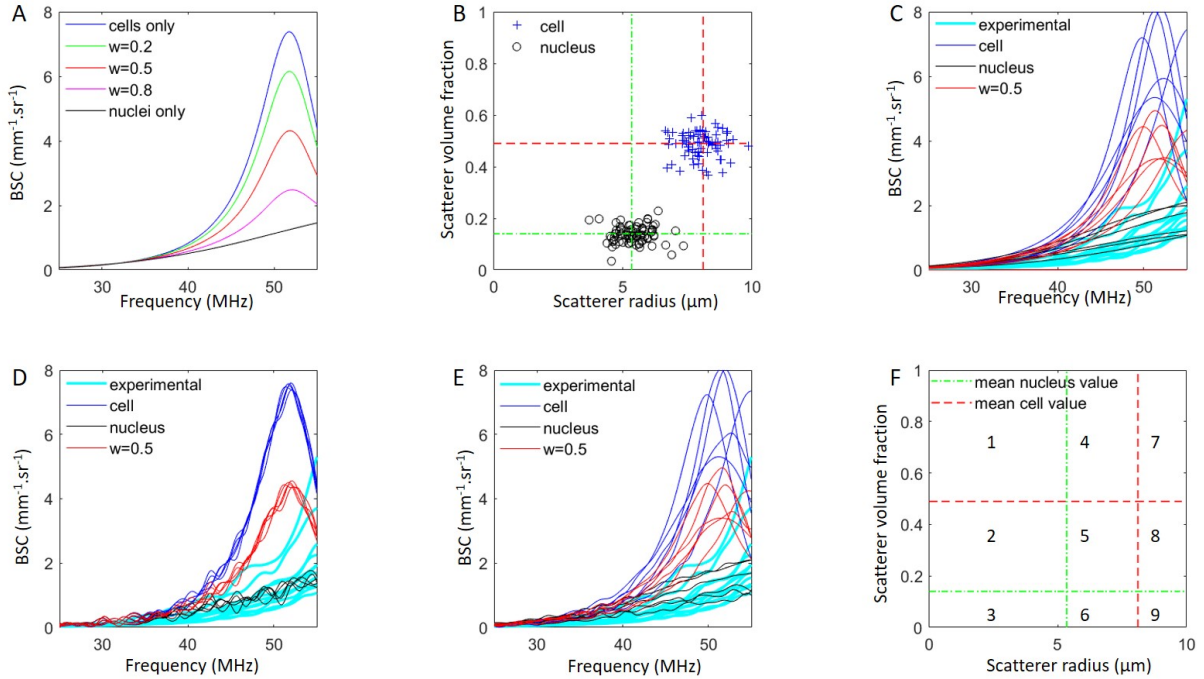


Fig. 4. A. Calculated BSCs for various nucleus/cell scattering ratios w for 4T1 CP. B. Using strategy 1, distribution of random nucleus and cell radii and volume fractions to theoretical BSCs for 4T1 CP. Superimposed examples of calculated BSCs and experimental BSCs for a 4T1 CP using strategy 1 (C), strategy 2 (D) and strategy 3 (E). F. Numbered a vs. ϕ grids for which green (a_N, ϕ_N) and red (a_C, ϕ_C) dashed lines correspond to the respective optical histology-derived mean values. CP denotes cell-pellet biophantom and T denotes tumor.

MAT CP was used. For tumors, γ_Z of 0.02 was used for 4T1 and JC T, 0.015 for LMTK T and 0.035 for MAT T. These γ_Z values were chosen by comparing calculated BSCs from nuclei and cells with the QUS-derived experimental BSCs for different γ_Z values (Figure 3). An example of calculated BSCs for scattering from cells only, nuclei only, and both cells and nuclei (for indicated values of w) is shown in Fig. 4A using optical histology-derived nucleus and cell a and ϕ values of 4T1 CP.

Three strategies were used to calculate the optical histology-derived BSCs. These calculated BSCs were used to estimate the optically derived scatterer parameters, by inversion using SFM, for scattering from nuclei only, cells only and both cells and nuclei. The comparison of the QUS-derived and optical histology-derived scatterer parameters will assist to determine if the scattering is from nuclei only, cells only or from both cells and nuclei for the cell type studied.

For strategy 1, 81 BSC_N (respectively, BSC_C) were generated using 81 uniform random a_N and ϕ_N (a_C and ϕ_C) values with a_N (a_C) ranging between $[\text{mean}(a_N) \pm \text{std}(a_N)]$ ($[\text{mean}(a_C) \pm \text{std}(a_C)]$) and with ϕ_N (ϕ_C) ranging between $[\text{mean}(\phi_N) \pm 0.25 \text{ mean}(\phi_N)]$ ($[\text{mean}(\phi_C) \pm 0.10 \text{ mean}(\phi_C)]$). An example of such an (a, ϕ) distribution for 4T1 CP is shown in Figure 4B for w ratios of 0 (cells only), 0.1, 0.2, 0.3, 0.4, 0.5, 0.6, 0.7, 0.8, 0.9 and 1 (nuclei only); note that nucleus values congregate around (a_N, ϕ_N) and cell values around (a_C, ϕ_C) . Eighty-one calculated BSC_{NC} were generated for each w ratio using the corresponding BSC_N

and BSC_C . An example of BSCs obtained for 4T1 CP with strategy 1 is shown in Figure 4C. The same inversion process with the minimization of the cost function (eq. 4), as used experimentally, was realized to estimate the optical histology-derived parameters.

For strategy 2, the mean nucleus and cell radii and volume fractions from each CP and T cell line were used to calculate BSC_N , BSC_C and BSC_{NC} . Uniform random noise was implemented to mimic BSC noise. The added noise had a mean of zero and a random variance increasing with frequency. The maximum variance increased from 1 to 5% of the maximum BSC from both cells and nuclei (with an w ratio of 0.5 of each structure). There were 81 realizations of noise for each cell line. A strategy 2 example of BSCs obtained for 4T1 CP is shown in Figure 4D. The same process, as used experimentally, was realized to estimate the optical histology-derived parameters.

Strategy 3 combined the generation of 81 BSC_N (BSC_C) with 81 uniform random a_N and ϕ_N (a_C and ϕ_C) and random noise to mimic experimental BSCs. A strategy 3 example of BSCs obtained for 4T1 CP is shown in Figure 4E. The same process, as used experimentally, was realized to estimate the optical histology-derived parameters.

The objective behind the evaluation of calculated BSCs and the optical histology-derived parameters is to understand the QUS-derived radius vs. volume fraction distributions. In particular, the effect of scattering from both cells and nuclei

evaluated with the monodisperse SFM is observed in these parameter distributions. The effect of noise on calculated BSCs is also taken into account in strategies 2 and 3.

III. RESULTS

A. Optical histology-derived tissue parameters of CP and T

The nucleus and cell radii and their volume fractions for each cell line were optically evaluated from histology images. These data are summarized in Table III. LMTK and MAT cell lines have smaller nucleus and cell radii than 4T1 and JC CP along with higher cell volume fractions. These nucleus and cell radii differences are smaller for T, along with no nucleus volume fraction differences. Also, no a_N/a_C ratio differences among these cell lines are noted.

The pink and blue contrast values of nuclei and cells for CP and T cell lines are shown in Figure 5. LMTK CP and JC T have pink contrast values of their nuclei and cells that are slightly higher than those of the other CP and T cell lines (Figure 5 A and C) along with lower blue contrast values (Figure 5 B and D). LMTK T has higher nucleus and cell blue contrast values compared to the other cell lines (Figure 5 B and D).

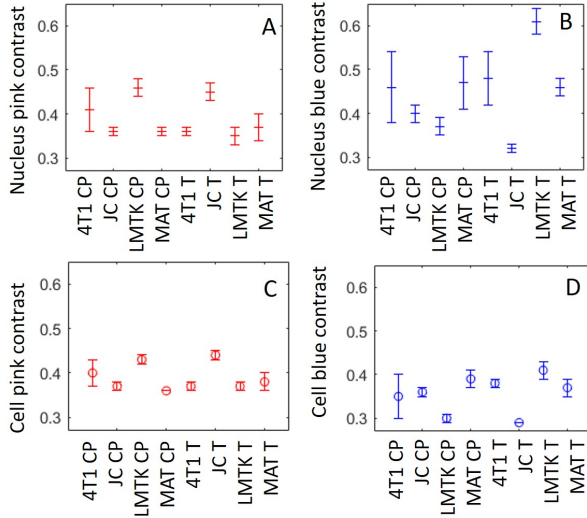


Fig. 5. Optical histology-derived pink and blue contrast estimates for the nucleus (A and B, respectively) and cell cytoplasm (C and D, respectively) for 4T1, JC, LMTK, and MAT CP and T. CP denotes cell-pellet biophantom and T denotes tumor

B. QUS-derived tissue parameters from BSC evaluations of CP and T

1) *Cell-pellet biophantoms*: The mean radii, volume fractions, and acoustic concentrations estimated from CP's QUS-derived BSCs using two QUS models (GM and SFM) are summarized in Table IV. Using SFM, LMTK and MAT radii and volume fractions have lower relative errors compared to cell optical histology-derived values ($\leq 14\%$ and $\leq 17\%$, respectively) than to nucleus optical histology-derived values.

4T1 and JC radii have low relative errors with nucleus radius ($\leq 10\%$ and $\leq 7\%$, respectively) and cell volume fraction ($\leq 2\%$ and $\leq 37\%$, respectively). Using GM, the four cell lines have small radii (close to $1 \mu\text{m}$) and large acoustic concentrations compared to SFM. The standard deviations provided by SFM are quite large, and observed on the (a, ϕ) scatterer parameter distributions (Figures 6A, 7A, 8A and 9A) with large outcome spreads.

2) *Ex vivo tumors*: The mean radii and volume fractions estimated from tumor's QUS-derived BSCs are summarized in Table V. All cell lines using the SFM have a small relative error for nucleus radii ($< 5\%$). However, even though the volume fractions are closer to nucleus volume fractions for 4T1, JC, MAT, and LMTK compared to cell volume fractions, the relative errors are quite high ($>90\%$ for 4T1, $>33\%$ for JC, $>52\%$ for LMTK and $>36\%$ for MAT). QUS-derived parameters evaluated with GM have quite good agreement with nuclei for the four cell lines (relative error from 1.48 to 20.87%). For JC, LMTK and MAT, SFM provides lower relative errors with nucleus radii than GM.

C. Comparison between QUS-derived a and ϕ from BSC measurements and optical histology-derived a and ϕ for CP and T cell lines

To describe (a, ϕ) distributions from experimental (QUS-derived from BSC measurements) and optical histology-derived parameters, the numbered grids presented in Figure 4F is used. For example, grid section 5 refers to outcomes with ϕ between ϕ_N and ϕ_C ($\phi_N < \phi_C$) and with a between a_N and a_C ($a_N < a_C$).

QUS-derived a and ϕ from experimental BSC measurements are directly compared with optical histology-derived a and ϕ on the a - ϕ nine-section grid (see Figures 4B and 4F). The a and ϕ axes are segmented by the mean a and ϕ cell and nucleus values derived from optical histology measurements and calculations. The notations on the a - ϕ grid are the a - ϕ coordinates that were derived experimentally from the QUS-derived BSC measurements and subsequent analysis strategies. For each CP and T cell line, the percentage of scatterers present in each of the nine sections was evaluated from QUS-derived and optical histology-derived a and ϕ values for cells only, nuclei only and both cells and nuclei. These two nine-set percentages were pair-wise evaluated using Matlab function *corrcoef* to yield the Pearson correlation coefficient R and then the best correlation coefficient for each CP and T cell line.

1) *QUS-derived scatterer parameter distributions*: The (a, ϕ) distributions from 4T1, JC, LMTK and MAT CP using SFM are presented in Figures 6A, 7A, 8A and 9A, respectively. The scatterer radii vs. volume fractions experimental inversions from 4T1 CP (Figure 6A) are mainly in sections 5 (30%), 3 (18%) and 1+4+7 (46%); from JC CP (Figure 7A) are mainly in sections 5 (63%) and 1+4 (13%);

Cell line	CP/T	a_N (μm)	ϕ_N	a_C (μm)	ϕ_C	a_N/a_C
4T1	CP	5.35 ± 0.56	0.14	8.12 ± 0.68	0.49	0.66
	T	4.96 ± 0.55	0.14	8.12*	0.64*	0.61*
JC	CP	5.49 ± 0.92	0.13	8.73 ± 1.85	0.52	0.63
	T	5.20 ± 0.71	0.14	8.73*	0.64*	0.60*
LMTK	CP	4.66 ± 0.46	0.15	7.25 ± 0.63	0.58	0.64
	T	4.62 ± 0.56	0.16	7.25*	0.64*	0.64*
MAT	CP	4.20 ± 0.41	0.13	7.25*	0.58*	0.60*
	T	4.37 ± 0.58	0.14	7.25*	0.65*	0.62*

TABLE III

OPTICAL HISTOLOGY-DERIVED NUCLEUS AND CELL RADII (a_N AND a_C , RESPECTIVELY) AND VOLUME FRACTIONS (ϕ_N AND ϕ_C , RESPECTIVELY), AS WELL AS NUCLEUS/CELL RADIUS RATIO a_N/a_C . a_N AND ϕ_N WERE EVALUATED FROM 4T1, JC, LMTK AND MAT CP AND T. a_C AND ϕ_C WERE EVALUATED FROM 4T1, JC, LMTK CP. FOR THE RADII VALUES, THE MEAN AND STANDARD DEVIATION ARE PRESENTED. THE SYMBOL * IS USED WHEN THE a_C VALUE WAS NOT POSSIBLE TO EXTRACT AND THAT THE a_C VALUE FROM ANOTHER CELL TYPE OR FROM CP WAS USED INSTEAD. a_C FROM 4T1 CP WAS USED FOR 4T1 T, a_C FROM JC CP WAS USED FOR JC T AND a_C FROM LMTK CP WAS USED FOR LMTK T, MAT CP AND MAT T. CP DENOTES CELL-PELLET BIOPHANTOM AND T DENOTES TUMOR.

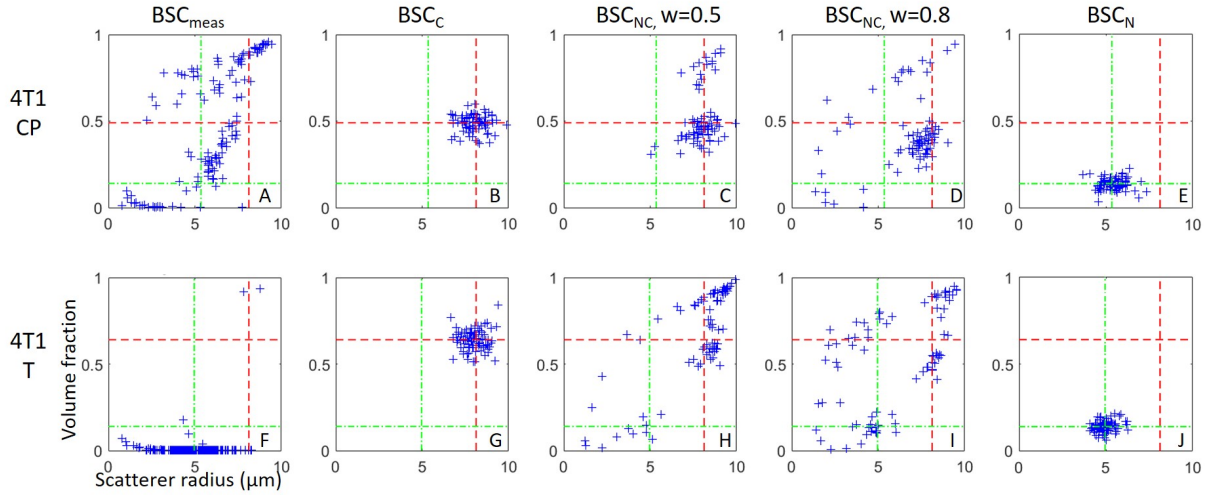


Fig. 6. 4T1 cell pellet (top row) and 4T1 tumor (bottom row) scatterer radius versus volume fraction from QUS-derived BSCs (first column, A and F), calculated cells-only BSCs (BSC_C , second column, B and G), calculated cells and nuclei BSCs for $w=0.5$ and 0.8 (BSC_{NC} , third and fourth column, C, D, H and I) and calculated nuclei-only BSCs (BSC_N , fifth column, E and J) obtained with strategy 1. The green (a_N & ϕ_N) and red (a_C & ϕ_C) dashed lines correspond to the mean optical histology-measured nucleus and cell radii and volume fractions, respectively. CP denotes cell-pellet biophantom and T denotes tumor.

from LMTK CP (Figure 8A) are mainly in sections 5+8 (53%) and 4+7 (34%); and from MAT CP (Figure 9A) are mainly in sections 5 (79%) and 7 (12%).

The scatterer radii vs. volume fractions experimental inversions from 4T1 T (Figure 6F) are mainly in sections 3+6 (98%); from JC T (Figure 7F) are mainly in sections 3+6 (76%) and 5 (18%); from LMTK T (Figure 8F) are mainly in sections 3+6 (84%) with a few in 1+4+7 (7%); and from MAT T (Figure 9F) are mainly in sections 3+6 (86%) with a few in 1+4+7 (11%).

2) *Strategy 1: random a and ϕ values:* The optically derived scatterer parameters presented in this subsection were obtained using strategy 1: calculated BSCs from random values of a and ϕ . The calculated BSC distributions from cell structures provide a and ϕ values close to those cell parameters evaluated optically from histology (Figures 6B and G, 7B and G, 8B and G and 9B and G). The calculated BSC distributions from nucleus structures provide a and ϕ values close to those nucleus parameters evaluated optically

from histology (Figures 6E and J, 7E and J, 8E and J and 9E and J). The calculated (a, ϕ) distributions from both nucleus and cell structures lead to outcomes especially in sections 3, 5 and 1+4+7 (Figures 6C-D and H-I, 7C-D and H-I, 8C-D and H-I and 9C-D and H-I).

The percentage of scatterers present in each grid section for scattering from cells only, nuclei only and both cells and nuclei were estimated, and their correlations with the experimental (a, ϕ) distributions are summarized in Table VI. For 4T1 and JC CP, these results highlight that the best correlations are for scattering from both cells and nuclei for which $w=0.9$ ($R=0.78$) for 4T1 and $w=0.8$ ($R=0.85$) for JC. LMTK and MAT CP present the best correlations for scattering from cells only ($R=0.64$ for LMTK and $R=0.59$ for MAT). 4T1, JC and MAT T present the best correlations for scattering from nuclei only ($R=0.46$ for 4T1, $R=0.81$ for JC, and $R=0.63$ for MAT). LMTK T present the best correlations for scattering from both cells and nuclei with $w=0.9$ ($R=0.46$).

The optically derived scatterer parameter distributions us-

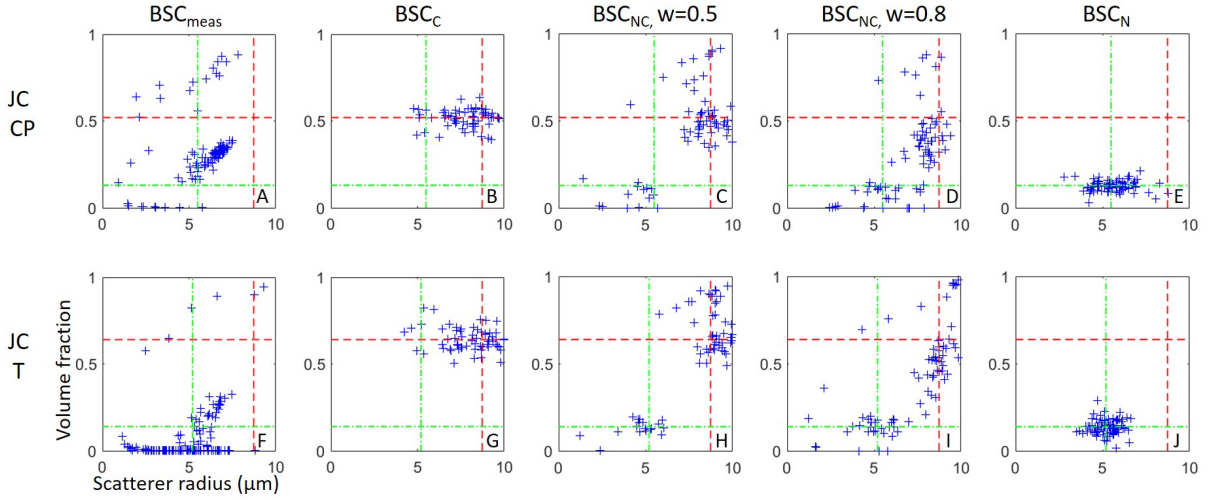


Fig. 7. JC cell pellet (top row) and JC tumor (bottom row) scatterer radius versus volume fraction from QUS-derived BSCs (first column, A and F), calculated cells-only BSCs (BSC_C , second column, B and G), calculated cells and nuclei BSCs for $w=0.5$ and 0.8 (BSC_{NC} , third and fourth column, C, D, H and I) and calculated nuclei-only BSCs (BSC_N , fifth column, E and J) obtained with strategy 1. The green (a_N & ϕ_N) and red (a_C & ϕ_C) dashed lines correspond to the mean optical histology-measured nucleus and cell radii and volume fractions, respectively. CP denotes cell-pellet biophantom and T denotes tumor.

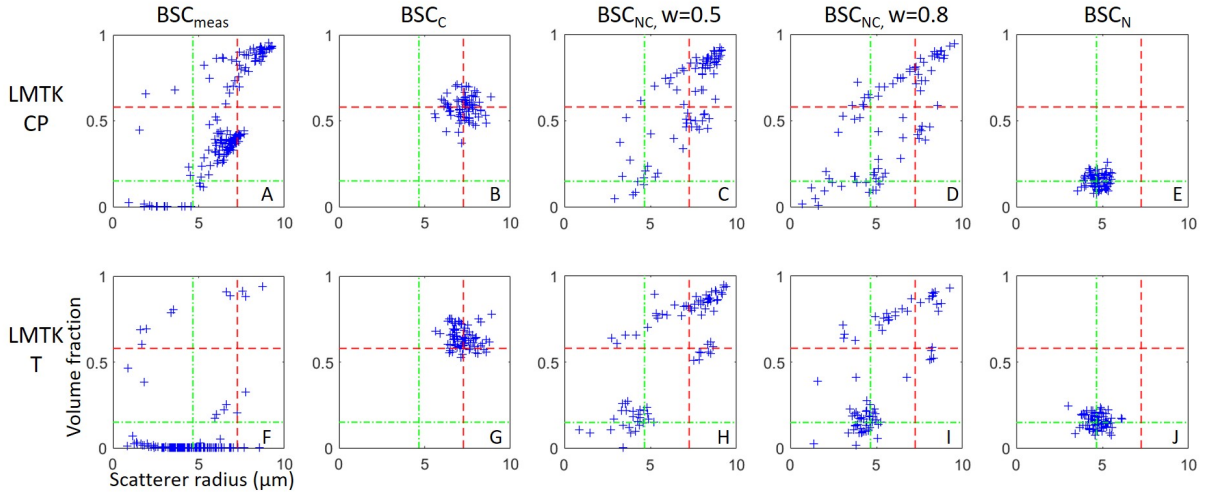


Fig. 8. LMTK cell pellet (top row) and LMTK tumor (bottom row) scatterer radius versus volume fraction from QUS-derived BSCs (first column, A and F), calculated cells-only BSCs (BSC_C , second column, B and G), calculated cells and nuclei BSCs for $w=0.5$ and 0.8 (BSC_{NC} , third and fourth column, C, D, H and I) and calculated nuclei-only BSCs (BSC_N , fifth column, E and J) obtained with strategy 1. The green (a_N & ϕ_N) and red (a_C & ϕ_C) dashed lines correspond to the mean optical histology-measured nucleus and cell radii and volume fractions, respectively. CP denotes cell-pellet biophantom and T denotes tumor.

ing strategies 2 and 3 are in Appendix (see supplementary materials).

IV. DISCUSSION

The study's approach is to gain insight into the histologically identifiable cellular structure(s) involved in ultrasonic scattering by considering two scattering models (spherical Gaussian Model: GM and Structure Factor Model: SFM) that yield quantitative measures of the nucleus and cell radii and their respective volume fractions (only for SFM). The general premise is that when ultrasonic scattering is assumed to be from nuclei only, the BSC is derived only from an incoherent contribution for which GM yields

reasonable nucleus size estimates. When ultrasonic scattering is assumed to be from cells only, the BSC is derived from both incoherent and coherent contributions for which SFM yields reasonable cell size estimates. And, when ultrasonic scattering is assumed to be from both cells and nuclei, a different approach is applied. Here, nucleus and cell radii (a_N, a_C) and their respective volume fractions (ϕ_N, ϕ_C) are derived optically from histology and used to calculate BSC for scattering from cells only, nuclei only and from both cells and nuclei. Optically derived scatterer parameters were evaluated from these calculated BSC and compared to the experimental QUS-derived a_N , a_C , ϕ_N and ϕ_C outcome parameters. This study evaluated four cell lines (4T1, JC,

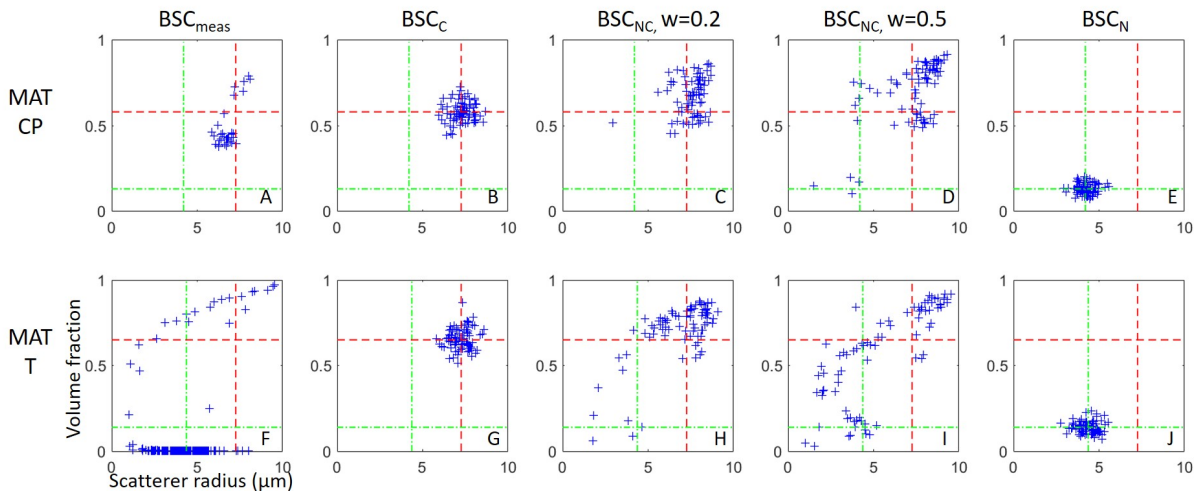


Fig. 9. MAT cell pellet (top row) and MAT tumor (bottom row) scatterer radius versus volume fraction from QUS-derived BSCs (first column, A and F), calculated cells-only BSCs (BSC_C , second column, B and G), calculated cells and nuclei BSCs for $w=0.2$ and 0.5 (BSC_{NC} , third and fourth column, C, D, H and I) and calculated nuclei-only BSCs (BSC_N , fifth column, E and J) obtained with strategy 1. The green (a_N & ϕ_N) and red (a_C & ϕ_C) dashed lines correspond to the mean optical histology-measured nucleus and cell radii and volume fractions, respectively. CP denotes cell-pellet biophantom and T denotes tumor.

CP cell line	QUS-derived parameters			Relative errors with nucleus (%)		Relative errors with cell (%)	
	a (μm)	ϕ	η_Z (dB/mm ³)	a_N	ϕ_N	a_C	ϕ_C
4T1 (SFM)	5.86 ± 2.14	0.48 ± 0.33	30.49 ± 14.22	9.46	255.11	25.33	1.46
4T1 (GM)	1.35 ± 1.24	-	52.56 ± 16.25	74.84	-	83.42	-
JC (SFM)	5.82 ± 1.54	0.33 ± 0.19	20.44 ± 12.57	6.01	152.92	33.33	36.77
JC (GM)	1.20 ± 0.86	-	53.95 ± 13.07	78.12	-	86.24	-
LMTK (SFM)	6.66 ± 1.68	0.50 ± 0.28	22.45 ± 14.84	42.92	234.53	8.14	13.48
LMTK (GM)	0.94 ± 0.73	-	56.68 ± 13.27	79.85	-	87.05	-
MAT (SFM)	6.81 ± 0.55	0.49 ± 0.13	15.77 ± 7.25	62.23	273.76	6.02	16.23
MAT GM	0.59 ± 0.05	-	66.32 ± 3.76	85.97	-	91.87	-

TABLE IV

QUS-DERIVED SCATTERER RADII a , VOLUME FRACTIONS ϕ AND ACOUSTIC CONCENTRATIONS η_Z ESTIMATED FROM EXPERIMENTAL BSCs OF 4T1, JC, LMTK, AND MAT CP USING SFM AND GM, THE 2 QUS MODELS. THE RELATIVE ERRORS COMPARE THE MEAN VALUES OF THE QUS-DERIVED PARAMETERS (a , ϕ) WITH THEIR RESPECTIVE OPTICAL HISTOLOGY-DERIVED NUCLEUS (a_N , ϕ_N) AND CELL (a_C , ϕ_C) PARAMETERS. CP DENOTES CELL-PELLET BIOPHANTOM.

LMTK and MAT) of both cell-pellet (CP) biophantoms and *ex vivo* tumors (T).

The first observation is that the QUS-derived (a, ϕ) distributions obtained for all cell lines and especially for CP are quite spread (Figure 6A, Figure 7A, Figure 8A, Figure 9A). Also, some of the tumor outcomes yield volume fractions close to zero which does not correspond to a physical scattering site (Figure 6F, Figure 7F, Figure 8F, Figure 9F). There are several considerations to explain volume fractions located near zero or a large distribution of the outcomes. 1) These outcome data may correspond to local minima, even if the minimal cost function were evaluated on 20 initial conditions. 2) There is neither a unique scattering structure (i.e., cell and nucleus) nor a monodisperse one that is not taken into account with the structure factor model.

A. Cellular structure(s) involved in ultrasonic scattering

Best correlations (Table VI) have assisted to identify which optical histology-derived (a, ϕ) distributions are closest to the QUS-derived (a, ϕ) distributions for cells only, nuclei only

and both cells and nuclei.

The Pearson's correlation coefficients between the optical histology-derived and QUS-derived (a, ϕ) distributions from *ex vivo* tumors of the four cell lines and the three analysis strategies (Table VI, Figures 6, 7, 8, 9) suggest that tumor scattering is mainly from nuclei, except for LMTK T for strategy 1 which provided a best correlation for scattering from both nuclei and cells.

The *ex vivo* tumors are thus considered dilute media because the scatterer parameter radius and acoustic concentration outcomes for both GM and SFM are similar [6], suggesting the dominance of incoherent backscattering. This observation is corroborated with the GM-evaluated scatterer radii being similar to the optical histology-derived nucleus radii (relative error between 1.48 and 20.87%, Table V). The SFM-evaluated scatterer radii are also close to the optical histology-derived nucleus radii (relative error between 0.60 and 4.92%, Table V). However, the nucleus volume fractions are quite different (relative error between 33.50 and 90.89%, Table V). It should be noted that for dilute media the Structure Function (S) is

T cell line	QUS-derived parameters			Relative errors with nucleus (%)		Relative errors with cell (%)	
	a (μm)	ϕ	η_Z (dB/mm ³)	a_N	ϕ_N	a_C	ϕ_C
4T1 (SFM)	4.82 \pm 1.33	0.01 \pm 0.09	11.82 \pm 9.21	4.47	90.89	41.64	98.01
4T1 (GM)	5.03 \pm 1.61	-	10.05 \pm 8.42	1.48	-	38.01	-
JC (SFM)	4.94 \pm 1.71	0.09 \pm 0.18	15.06 \pm 12.56	4.92	33.50	43.37	85.45
JC (GM)	4.11 \pm 2.02	-	19.00 \pm 15.00	20.87	-	52.87	-
LMTK (SFM)	4.40 \pm 1.70	0.08 \pm 0.22	13.59 \pm 13.32	4.67	52.55	39.25	88.14
LMTK (GM)	4.19 \pm 1.94	-	13.00 \pm 12.28	9.26	-	42.18	-
MAT (SFM)	4.34 \pm 1.54	0.09 \pm 0.25	19.14 \pm 12.93	0.60	36.54	40.09	86.94
MAT (GM)	3.98 \pm 1.76	-	19.13 \pm 14.28	8.91	-	45.10	-

TABLE V

QUS-DERIVED SCATTERER RADII a , VOLUME FRACTIONS ϕ AND ACOUSTIC CONCENTRATIONS η_Z ESTIMATED FROM EXPERIMENTAL BSCS OF 4T1, JC, LMTK, AND MAT T USING SFM AND GM, THE 2 QUS MODELS. THE RELATIVE ERRORS COMPARE THE MEAN VALUES OF THE QUS-DERIVED PARAMETERS (a , ϕ) WITH THEIR RESPECTIVE OPTICAL HISTOLOGY-DERIVED NUCLEUS (a_N , ϕ_N) AND CELL (a_C , ϕ_C) PARAMETERS. T DENOTES TUMOR.

	Strategy 1		Strategy 2		Strategy 3	
	best R	corresponding w	best R	corresponding w	best R	corresponding w
4T1 CP	0.77	0.9, NC	0.68	0.1, NC	0.74	0.8, NC
4T1 T	0.46	1, N	0.31	1, N	0.41	1, N
JC CP	0.85	0.8, NC	0.97	0.4, NC	0.93	1, N
JC T	0.81	1, N	0.58	1, N	0.49	1, N
LMTK CP	0.64	0, C	0.88	0, C	0.80	0.1, NC
LMTK T	0.46	0.9, NC	0.20	1, N	0.25	1, N
MAT CP	0.59	0, C	0.69	0, C	0.69	1, N
MAT T	0.63	1, N	0.19	1, N	0.11	1, N

TABLE VI

BEST CORRELATION COEFFICIENTS (PEARSON R) BETWEEN THE PERCENTAGE OF NUMERICAL SCATTERERS PRESENT IN EACH GRID SECTION (FIGURE 4F) FOR SCATTERING FROM CELLS ONLY, NUCLEI ONLY AND BOTH CELLS AND NUCLEI WITH THE EXPERIMENTAL (a , ϕ) DISTRIBUTION FOR EACH CP AND T CELL LINES (CP/T). CP DENOTES CELL-PELLET BIOPHANTOM, T DENOTES TUMOR, N DENOTES NUCLEI ONLY, C DENOTES CELLS ONLY AND NC DENOTES BOTH NUCLEI AND CELLS.

close to unity, which leads to challenges extracting correctly the scatterer volume fraction and relative impedance contrast from the acoustic concentration.

The Pearson's correlation coefficients between optical histology-derived and QUS-derived (a , ϕ) distributions from LMTK and MAT CP with strategies 1 and 2 (Table VI, Figure 8, Figure 9) suggest scattering from cells only. However, for strategy 3, the best correlation for LMTK CP is for scattering from both nuclei and cells and the best correlation for MAT CP is for scattering from nuclei only. Similarly, the best correlations between optical histology-derived and QUS-derived (a , ϕ) distributions from 4T1 and JC CP with strategies 1 and 2 (Table VI, Figure 6, Figure 7) suggest scattering from both cells and nuclei. Strategy 3 provides the best correlation for 4T1 CP for scattering from both nuclei and cells but the best correlation for JC CP is for scattering from nuclei only. Based on these observations, strategy 3 (includes variations from a and ϕ values as well as from adding noise) may not be appropriate for comparison of experimental results.

The CP biophantoms are considered dense media because the GM-evaluated scatterer radii are underestimated and the acoustic concentrations are overestimated [6], suggesting that both incoherent and coherent backscatter components are present. Moreover, the GM-evaluated scatterer radius is close to 1 μm (Table IV), thus not corresponding neither to nucleus nor to cell radii. The optical histology-derived nucleus volume fractions are similar between CP and T, suggesting for the CP case that either cell structure or both nucleus and cell structures are involved in ultrasonic scattering. The

mean MAT and LMTK CP scatterer optical histology-derived parameters are similar to whole cell parameters (relative error $\leq 17\%$, Table IV). The mean 4T1 and JC CP scatterer radius parameters are similar to the optical histology-derived nucleus radii (relative error $< 10\%$) but the volume fraction estimates are quite different from optical histology-derived nucleus volume fractions (relative error $> 152\%$) and closer to the cell volume fractions (relative error $< 37\%$, Table IV).

As a concluding comment, the (a , ϕ) distribution results with strategies 1 and 2 are (almost) in agreement with the mean scatterer parameters (Tables IV, V and VI). These results suggest that nuclei only are the main structure involved in ultrasonic scattering from 4T1, JC, LMTK and MAT T, that cells only are the main structure involved in ultrasonic scattering from LMTK and MAT CP and that both cells and nuclei are involved in ultrasonic scattering from 4T1 and JC CP.

B. Differences between CP and T that may explain a difference in the structure involved in ultrasonic scattering

The scattering structures are different between CP and T, CP providing insight into dense media and T providing insight into dilute media. Moreover, if the nucleus appears to be a major scattering source from 4T1 and JC CP and T, then for LMTK and MAT a difference in the scatterer source is observed with cells for CP and nuclei for T.

The nucleus radii from T shows a slight increase for LMTK and MAT compared to CP along with a slight

decrease of 4T1 and JC CP, reducing the radii differences among 4T1/JC and LMTK/MAT (Table III). There are no contrast differences between 4T1/JC and LMTK/MAT which may explain a change of scattering structure for LMTK and MAT (Figure 5). However, the main difference between CP and T may be the cell relative impedance contrast, γ_Z . Indeed, from histology images of CP, spaces are observed between cells (Figures 2A-D). These spaces are certainly filled with DPBS/saline during ultrasonic acquisitions. For T (Figures 2E-H), there are no spaces between cells, so the surrounding medium of cells is certainly occupied by other cytoplasm and eventually extracellular matrix, possibly leading to a lower relative impedance contrast between cells, and certainly much lower than the relative impedance contrast between cytoplasm and DPBS/saline from CP. This may explain why the scattering structure from MAT and LMTK T is not the cell (or both cell and nucleus) and why there may be no contribution of the cell for 4T1 and JC T.

This difference in the structure involved in ultrasonic scattering from CP and T of the same cell line suggests that the CP (at least for the four cell lines evaluated herein) may not be good tumor models. The use of spheroids of cells with extracellular matrix presence and cell interactions may provide a better tumor model.

C. Limits of the study

Two ultrasonic scattering models (GM and SFM) were used to elucidate the scattering mechanism(s). Both models assumed monodisperse scatterers. Polydisperse models, and perhaps a wider range of models, should be included in future studies to further assist with mechanistic understanding of ultrasonic scattering. Optical histology-derived parameter outcomes were compared to QUS-derived parameter outcomes from experimental BSCs. To generate these calculated BSC, a combination of BSC from nuclei and cells was used (Eq 7). The nucleus and cell radii and volume fractions were optically estimated. However, the relative impedance contrast was chosen to be identical for cells and nuclei which poses a serious limitation particularly as it also can affect the nucleus/cell scattering ratio w term. A future improvement could be the addition of a direct impedance contrast assessment using acoustic microscopy, for example [24], [25].

Correlation analyses between QUS-derived (a, ϕ) parameter outcomes and optical histology-derived (a, ϕ) parameter outcomes were performed utilizing the a vs. ϕ nine-section grid (Figure 4F). On this grid, the a and ϕ axes were segmented by the mean a and ϕ cell and nucleus values. However, with this definition, an outcome close to cell radii and volume fractions may be in section 4, 5, 7 or 8 and an outcome close to nucleus radii and volume fractions may be in section 2, 3, 5 or 8. The correlation of the percentage of outcomes in each grid section could then introduce a bias if there were a shift of the outcome positions. Other analysis

approaches might provide more robust a - ϕ distributions.

To obtain insight about the cellular structure(s) involved in ultrasonic scattering this study was conducted using simple models containing mostly cells: cell-pellet biophantoms containing cells only and the *ex vivo* tumors containing cells and also extracellular matrix. For *in vivo* tumors, the presence of blood vessels, connective tissue and lymphatic structures would affect the scattering, likely resulting in more complex scattering. Such additional intercellular materials would likely lead to QUS-derived parameter outcomes more difficult to interpret and compare with optical histology-measured data, even with a monodisperse model.

V. CONCLUSION

The study's objective was to gain insight into specific cellular structure(s) involved in ultrasonic scattering. Indeed, there is significant scientific value to elucidate the ultrasonic scattering structure(s), particularly at the cellular scale to determine for example if CP biophantoms are equivalent models of *ex vivo* tumors for tissue characterization applications. Ultrasonic scatterer parameters from four cell lines of cell-pellet biophantoms and *ex vivo* tumors were evaluated using two scattering models (SFM and GM) and compared to the optical histology-measured parameters (cells and nuclei radii and volume fractions) to evaluate if the structure(s) involved in ultrasonic scattering is(are) cells only or nuclei only. To determine if both cells and nuclei were involved in ultrasonic scattering, BSCs were calculated using a simple model with the optical histology-measured parameters as inputs. The optical histology scatterer parameter distributions derived from these calculated BSCs were compared to the QUS-derived scatterer parameters. The results highlight that nuclei appear to be the main structure involved in ultrasonic scattering for 4T1, JC, LMTK, and MAT tumors; that cells appear to be the structure involved in ultrasonic scattering for LMTK and MAT cell pellets; and that cells and nuclei appear to be the structures involved in ultrasonic scattering for 4T1 and JC cell pellets. In future studies, the cellular structure(s) involved in ultrasonic scattering may be evaluated for more cell lines to further elucidate scattering structure(s) from one cell line to another. The evaluation of the cellular structure(s) involved in ultrasonic scattering should also involve *in vivo* tumors.

VI. ACKNOWLEDGMENTS

We thank Rita Miller, DVM, Jamie Kelly, Jake Berndt, and Professor Aiguo Han for their help with cell culture, animal care and ultrasonic acquisitions.

REFERENCES

- [1] A. Han, R. Abuhabsah, J. P. Blue, S. Sarwate, and W. D. O'Brien, "Ultrasonic backscatter coefficient quantitative estimates from high-concentration Chinese hamster ovary cell pellet biophantoms," *The Journal of the Acoustical Society of America*, vol. 130, no. 6, pp. 4139–4147, Dec. 2011. [Online]. Available: <https://asa.scitation.org/doi/abs/10.1121/1.3655879>

- [2] A. Han, R. Abuhabsah, R. J. Miller, S. Sarwate, and W. D. O'Brien, "The measurement of ultrasound backscattering from cell pellet biophantoms and tumors ex vivo," *The Journal of the Acoustical Society of America*, vol. 134, no. 1, pp. 686–693, Jul. 2013, publisher: Acoustical Society of America. [Online]. Available: <https://asa.scitation.org/doi/abs/10.1121/1.4807576>
- [3] A. Han and W. D. O'Brien, "Structure function for high-concentration biophantoms of polydisperse scatterer sizes," *IEEE Transactions on Ultrasonics, Ferroelectrics, and Frequency Control*, vol. 62, no. 2, pp. 303–318, Feb. 2015, conference Name: IEEE Transactions on Ultrasonics, Ferroelectrics, and Frequency Control.
- [4] E. Franceschini and R. Guillermin, "Experimental assessment of four ultrasound scattering models for characterizing concentrated tissue-mimicking phantoms," *The Journal of the Acoustical Society of America*, vol. 132, no. 6, pp. 3735–3747, Dec. 2012, publisher: Acoustical Society of America. [Online]. Available: <https://asa.scitation.org/doi/abs/10.1121/1.4765072>
- [5] E. Franceschini, R. Guillermin, F. Tourniaire, S. Roffino, E. Lamy, and J.-F. Landrier, "Structure factor model for understanding the measured backscatter coefficients from concentrated cell pellet biophantoms," *The Journal of the Acoustical Society of America*, vol. 135, no. 6, pp. 3620–3631, Jun. 2014, publisher: Acoustical Society of America. [Online]. Available: <https://asa.scitation.org/doi/abs/10.1121/1.4876375>
- [6] E. Franceschini, R. d. Monchy, and J. Mamou, "Quantitative Characterization of Tissue Microstructure in Concentrated Cell Pellet Biophantoms Based on the Structure Factor Model," *IEEE Transactions on Ultrasonics, Ferroelectrics, and Frequency Control*, vol. 63, no. 9, pp. 1321–1334, Sep. 2016, conference Name: IEEE Transactions on Ultrasonics, Ferroelectrics, and Frequency Control.
- [7] A. Cristea, E. Franceschini, F. Lin, J. Mamou, C. Cachard, and O. Basset, "Quantitative Characterization of Concentrated Cell Pellet Biophantoms using Statistical Models for the Ultrasound Echo Envelope," *Physics Procedia*, vol. 70, pp. 1091–1095, Jan. 2015. [Online]. Available: <http://www.sciencedirect.com/science/article/pii/S1875389215009748>
- [8] G. J. Czarnota and M. C. Kolios, "Ultrasound detection of cell death," *Imaging in Medicine*, vol. 2, no. 1, pp. 17–28, Feb. 2010, publisher: Open Access Journals. [Online]. Available: <https://www.openaccessjournals.com/abstract/ultrasound-detection-of-cell-death-10977.html>
- [9] R. M. Vlad, R. K. Saha, N. M. Alajez, S. Ranieri, G. J. Czarnota, and M. C. Kolios, "An Increase in Cellular Size Variance Contributes to the Increase in Ultrasound Backscatter During Cell Death," *Ultrasound in Medicine & Biology*, vol. 36, no. 9, pp. 1546–1558, Sep. 2010. [Online]. Available: <http://www.sciencedirect.com/science/article/pii/S0301562910002553>
- [10] M. C. Kolios, G. J. Czarnota, M. Lee, J. W. Hunt, and M. D. Sherar, "Ultrasound spectral parameter characterization of apoptosis," *Ultrasound in Medicine & Biology*, vol. 28, no. 5, pp. 589–597, May 2002. [Online]. Available: <http://www.sciencedirect.com/science/article/pii/S0301562902004921>
- [11] R. M. Vlad, N. M. Alajez, A. Giles, M. C. Kolios, and G. J. Czarnota, "Quantitative Ultrasound Characterization of Cancer Radiotherapy Effects In Vitro," *International Journal of Radiation Oncology*Biophysics*Physics*, vol. 72, no. 4, pp. 1236–1243, Nov. 2008. [Online]. Available: <http://www.sciencedirect.com/science/article/pii/S0360301608031131>
- [12] P. Muleki-Seya, R. Guillermin, J. Guglielmi, J. Chen, T. Pourcher, E. Konofagou, and E. Franceschini, "High-Frequency Quantitative Ultrasound Spectroscopy of Excised Canine Livers and Mouse Tumors Using the Structure Factor Model," *IEEE Transactions on Ultrasonics, Ferroelectrics, and Frequency Control*, vol. 63, no. 9, pp. 1335–1350, Sep. 2016.
- [13] D. Savéry and G. Cloutier, "A point process approach to assess the frequency dependence of ultrasound backscattering by aggregating red blood cells," *The Journal of the Acoustical Society of America*, vol. 110, no. 6, pp. 3252–3262, Dec. 2001, publisher: Acoustical Society of America. [Online]. Available: <https://asa.scitation.org/doi/abs/10.1121/1.1419092>
- [14] V. Twersky, "Low-frequency scattering by correlated distributions of randomly oriented particles," *The Journal of the Acoustical Society of America*, vol. 81, no. 5, pp. 1609–1618, May 1987, publisher: Acoustical Society of America. [Online]. Available: <https://asa.scitation.org/doi/abs/10.1121/1.394513>
- [15] A. D. Pawlicki, A. J. Dapore, S. Sarwate, and W. D. O'Brien, "Three-dimensional impedance map analysis of rabbit liver," *The Journal of the Acoustical Society of America*, vol. 130, no. 5, pp. EL334–EL338, Oct. 2011, publisher: Acoustical Society of America. [Online]. Available: <https://asa.scitation.org/doi/full/10.1121/1.3646024>
- [16] L. R. Taggart, R. E. Baddour, A. Giles, G. J. Czarnota, and M. C. Kolios, "Ultrasound Characterization of Whole Cells and Isolated Nuclei," *Ultrasound in Medicine & Biology*, vol. 33, no. 3, pp. 389–401, Mar. 2007. [Online]. Available: <https://www.sciencedirect.com/science/article/pii/S0301562906017790>
- [17] J. W. Hunt, A. E. Worthington, and A. T. Kerr, "The subtleties of ultrasound images of an ensemble of cells: simulation from regular and more random distributions of scatterers," *Ultrasound in Medicine & Biology*, vol. 21, no. 3, pp. 329–341, Jan. 1995. [Online]. Available: <http://www.sciencedirect.com/science/article/pii/0301562994001203>
- [18] G. J. Czarnota, M. C. Kolios, H. Vaziri, S. Benchimol, F. P. Ottensmeyer, M. D. Sherar, and J. W. Hunt, "Ultrasound biomicroscopy of viable, dead and apoptotic cells," *Ultrasound in Medicine & Biology*, vol. 23, no. 6, pp. 961–965, Jan. 1997. [Online]. Available: <http://www.sciencedirect.com/science/article/pii/S0301562997000677>
- [19] G. J. Czarnota, M. C. Kolios, J. Abraham, M. Portnoy, F. P. Ottensmeyer, J. W. Hunt, and M. D. Sherar, "Ultrasound imaging of apoptosis: high-resolution non-invasive monitoring of programmed cell death in vitro, in situ and in vivo," *British Journal of Cancer*, vol. 81, no. 3, pp. 520–527, Oct. 1999, number: 3 Publisher: Nature Publishing Group. [Online]. Available: <https://www.nature.com/articles/6690724>
- [20] K. A. Wear, T. A. Stiles, G. R. Frank, E. L. Madsen, F. Cheng, E. J. Feleppa, C. S. Hall, B. S. Kim, P. Lee, W. D. O'Brien, M. L. Oelze, B. I. Raju, K. K. Shung, T. A. Wilson, and J. R. Yuan, "Interlaboratory Comparison of Ultrasound Backscatter Coefficient Measurements From 2 to 9 MHz," *Journal of Ultrasound in Medicine*, vol. 24, no. 9, pp. 1235–1250, 2005. [Online]. Available: <https://onlinelibrary.wiley.com/doi/abs/10.7863/jum.2005.24.9.1235>
- [21] J. Mamou, M. L. Oelze, W. D. O'Brien, and J. F. Zachary, "Identifying ultrasonic scattering sites from three-dimensional impedance maps," *The Journal of the Acoustical Society of America*, vol. 117, no. 1, pp. 413–423, Jan. 2005, publisher: Acoustical Society of America. [Online]. Available: <https://asa.scitation.org/doi/abs/10.1121/1.1810191>
- [22] M. F. Insana, D. G. Brown, K. K. Shung *et al.*, "Acoustic scattering theory applied to soft biological tissues," *Ultrasonic scattering in biological tissues*, pp. 75–124, 1993.
- [23] M. S. Wertheim, "Exact Solution of the Percus-Yevick Integral Equation for Hard Spheres," *Physical Review Letters*, vol. 10, no. 8, pp. 321–323, Apr. 1963, publisher: American Physical Society. [Online]. Available: <https://link.aps.org/doi/10.1103/PhysRevLett.10.321>
- [24] N. Hozumi, S. Yoshida, and K. Kobayashi, "Three-dimensional acoustic impedance mapping of cultured biological cells," *Ultrasonics*, vol. 99, p. 105966, Nov. 2019. [Online]. Available: <https://www.sciencedirect.com/science/article/pii/S0041624X18306486>
- [25] E. B. Prastika, A. Imori, T. Kawashima, Y. Murakami, N. Hozumi, S. Yoshida, R. Nagaoka, and K. Kobayashi, "Three-dimensional acoustic impedance mapping of human skin by improved time–frequency domain analysis," *Japanese Journal of Applied Physics*, vol. 60, no. SD, p. SDDE22, May 2021, publisher: IOP Publishing. [Online]. Available: <https://doi.org/10.35848/1347-4065/abf512>